*Conference on Modelling Fluid Flow (CMFF'25)*
*The 19th International Conference on Fluid Flow Technologies*
*Budapest, Hungary, August 26 - August 29, 2025*

# A COMPRESSIBLE TWO-FLUID MODEL FOR THE SIMULATION OF TRIBOELECTRIFICATION

Jürgen Abraham[2], Martin Gruber[3], Alexander Kospach[2], Mohammadsadegh Salehi[2], Stefan Radl[1]

[1] Corresponding Author. Institute of Process and Particle Engineering, Graz University of Technology. Inffeldgasse 13/III, Graz, Austria. Tel.: +43 316 873 - 30412, E-mail: radl@tugraz.at
[2] Virtual Vehicle Research GmbH, Inffeldgasse 21A, Graz, E-mail: Jürgen.Abraham@v2c2.at
[3] Institute of Process and Particle Engineering, Graz University of Technology. Inffeldgasse 13/III, Graz, Austria. E-mail: martin.gruber@tugraz.at

## ABSTRACT

Electrostatic interactions in compressible particle-laden flows are relevant for applications ranging from lithium-ion batteries to industrial dust explosions. Currently, their simulation remains challenging because charge transport must be resolved alongside steep gas density gradients and turbulence. Our present contribution augments an existing compressible two-fluid framework in OpenFOAM® with a function object that predicts net particle charge. The model's fidelity is demonstrated in two unit tests: unit test 1 isolates diffusive and conductive terms in a planar channel, and shows good agreement with corresponding analytical solutions. Unit test 2 benchmarks the enhanced two-fluid solver against a single-phase reference solution in a converging-diverging nozzle. A showcase simulation then tracks charge build-up and electric-field hotspots in a turbulent particle plume.

The resulting function object enables predictive studies of potentially arc-triggering charge accumulation in relevant flow scenarios, e.g., during thermal runaway of batteries. Also, ignition risks in pneumatic powder transport, volcanic-ash electrification, or other safety-relevant configurations can be assessed with our tool.

**Keywords: CFD, compressible flow, triboelectrification, two-fluid model, gas-particle flow**

## NOMENCLATURE

**Latin symbols**

| | | |
|---|---|---|
| $d$ | $[m]$ | diameter |
| **E** | $[\frac{kg\ m}{s^3\ A}]$ | electric field |
| $e$ | $[C = A \cdot s]$ | electron charge |
| $L$ | $[m]$ | characteristic system length |
| $m$ | $[kg]$ | mass |
| $M$ | $\left[\frac{kg}{kmol}\right]$ | molar mass |
| $n$ | $[-]$ | inward normal of the wall |
| $p$ | $[Pa]$ | pressure |
| $Q$ | $[A \cdot s]$ | mean charge of particles |
| $r$ | $[m]$ | radius |
| R | $[\frac{J}{kmol\ K}]$ | universal gas constant |
| $T$ | $[K]$ | temperature |
| $t$ | $[s]$ | time |
| **u** | $\left[\frac{m}{s}\right]$ | velocity vector |
| $V$ | $[m^3]$ | volume |
| $x$ | $[m]$ | axial position |

**Greek symbols**

| | | |
|---|---|---|
| $\alpha$ | [-] | volume fraction |
| δ | [m] | electron tunnelling distance |
| Δφ | $[eV]$ | work function difference |
| $\varepsilon_0$ | $\left[\frac{F}{m}\right]$ | vacuum permittivity |
| $\theta$ | $\left[\frac{m^2}{s^2}\right]$ | granular temperature |
| $\kappa_p$ | $\left[\frac{m^2}{s}\right]$ | thermal diffusivity |
| $\kappa_q$ | $\left[\frac{1}{ms}\right]$ | triboelectric diffusivity |
| $\rho$ | $\left[\frac{kg}{m^3}\right]$ | density |
| $\sigma$ | $\left[\frac{S}{m}\right]$ | triboelectric conductivity |

**Subscripts and Superscripts**

| | |
|---|---|
| $c$ | contact point |
| $e$ | exit (nozzle outlet) |
| $g$ | gas phase |
| $p$ | particle (solid) phase |
| $q$ | triboelectric (charge-related) |

| | |
|---|---|
| *t* | total |
| *w* | wall |
| *e* | exit (nozzle outlet) |
| *0* | stagnation/total condition |
| * | (i) non-dimensionalised variable (e.g $x^*$,$t^*$)<br>(ii) effective quantity (e.g $r^*$) |

## 1 INTRODUCTION

Triboelectrification occurs in gas–particle systems when collisions and frictional contacts transfer charge between solid surfaces, resulting in additional cohesive forces and localized electric fields. When gas is released rapidly, these fields can initiate arcing events that damage equipment or ignite flammable mixtures [1], [2]. In addition, at speeds above Mach 0.3, the compressibility of the gas phase may lead to shock formation and rapid expansions that drive transient variations in density and enthalpy, amplify pressure and temperature peaks, and produce nonlinear wave interactions. Resolving these phenomena therefore requires considering the full compressible flow equations. Such charging behavior under high-speed, compressible conditions has been observed in lithium-ion battery venting [3], volcanic ash plumes [4], planetary dust storms [5], and pneumatic powder conveying [2], [6].

To predict net charge generation in these flows, particle-resolved CFD–DEM simulations resolve every contact. However, they are impractical for a high amount of particles due to the cost of collision resolution [7]. Continuum Euler–Euler two-fluid models address this limitation by treating gas and particles as interpenetrating continua, and simulate net particle charge transport with an additional scalar transport equation. This approach lowers the computational expense for large particle counts while retaining the essential coupling of flow dynamics, charge transport and cohesive forces [8].

Experimental efforts have quantified triboelectric charging under flow conditions using both single-particle rigs and bulk powder measurements. Xu and Grosshans measured peak net charges at intermediate humidity in a PMMA duct [9], Cruise et al. demonstrated that air breakdown limits surface-charge saturation in pressure-chamber tests [10], and Liu et al. employed a contact–separation triboelectric nanogenerator in high vacuum to isolate intrinsic surface-charge densities free of gas-phase losses [11].

Building on these findings, CFD–DEM frameworks now allow incorporating triboelectric contact models with turbulent powder flows. For example, Alfano et al. coupled DEM collision models to a compressible RANS solver in an aerodynamic powder disperser and confirmed material-specific charge-to-area ratios against experiments [12]. Grosshans applied four-way coupled Euler–Lagrange simulations to show that even weak electrostatic charges markedly enhance near-wall particle clustering in pneumatic conveying, with secondary vortices modulating rather than negating this effect [13].

More recently, Euler–Euler models have advanced continuum tribocharging modeling by including charge–momentum coupling, polydispersity, and compressible effects. For example, Zeybek and Grosshans proposed a DQMOM-based scheme that discretizes the joint size–velocity–charge distribution, closes wall-contact and particle-particle charge-transfer terms with kinetic theory-based models, and solves Poisson's equation for the volumetric charge field, reproducing the formation and diffusion of a sharp charge boundary layer whose characteristics depend on particle-size distribution and charge diffusivity [14]. Montilla et al. derived second-order moment equations for the charge–velocity covariance and charge variance, as well as demonstrated that including the covariance transport improves predictions of charge diffusion in unsteady flows [15]. Ray et al. developed mean-charge transport equations for bi-disperse systems and showed in one-dimensional simulations that size disparity alone can induce spontaneous bipolar charging for identical materials [16].

While recent advances in CFD–DEM and Euler–Euler models have enabled triboelectric simulations under turbulent and compressible conditions, critical gaps remain in the field of open-source, compressible two-fluid simulation frameworks: existing implementations often rely on in-house codes or lack integration with finite-volume solvers for reactive multiphase flows, limiting accessibility and scalability. Moreover, the interplay between compressibility effects (e.g., shocks, rapid expansions) and tribocharging dynamics – expected to be of key importance in applications like battery venting or volcanic plumes - has not been rigorously investigated with continuum-based solvers.

To address these challenges, we present a generalized charge transport function object for OpenFOAM®'s „reactingTwoPhaseEulerFoam" solver, verified for conductive/diffusive limits and in compressible nozzle flow. Also, we showcase the solver in a forward-facing step flow. Thereby, our work bridges the gap between high-fidelity triboelectric models and open-source multiphase CFD, enabling studies of charge-momentum coupling in industrially relevant geometries.

The remainder of our contribution is organised as follows: Section 2 details the governing equations, numerical implementation, and boundary conditions. Section 3 verifies the charge-transport with conductive and diffusive benchmarks, while in Section 4, a showcase is presented. Section 5 summarises the main conclusions and outlines future work.

## 2 METHODOLOGY

This section summarizes the governing compressible two-fluid and charge-transport equations, their implementation in OpenFOAM®, and the boundary-condition in this study. We note in passing that in our present study $x^*$ and $t^*$ denote non-dimensional variables, whereas $r^*$ indicates the effective particle radius.

### 2.1 Flow

The Eulerian-Eulerian approach was applied in the present study to simulate a gas-particle flow system in OpenFOAM®. Two-Fluid Model (TFM) is also termed „Eulerian-Eulerian" approach since different phases are treated mathematically as interpenetrating continua. In this approach, conservation equations are solved for each phase, and these equations are linked by an interphase momentum transfer coefficient and the gas pressure. The interphase momentum exchange was modeled using the drag law proposed by Wen and Yu [17]. Besides this, the kinetic theory of granular flow, as well as a frictional model, was adopted to close the solid-phase stress tensor. Finally, the no-slip boundary condition was used for the gas phase, and the solid-phase transport equations are closed using the Johnson & Jackson boundary condition [18]. The full governing equations - including those for thermal energy – are standard, and will be shared by the authors upon reasonable request.

### 2.2 Charge transport equations

The following equation has been implemented in the form of a function object in the OpenFOAM® software environment to solve the charge transport equation:

$$\partial_t\left(\frac{\alpha_p}{V_p}Q_p\right)+\boldsymbol{\nabla}\cdot\left(\frac{\alpha_p}{V_p}Q_p\mathbf{u_p}\right)=-\sigma_q\frac{\alpha_pQ_p}{\varepsilon_0V_p}+\boldsymbol{\nabla}\cdot(\kappa_{total}\boldsymbol{\nabla}Q_p) \quad (1)$$

Here the following definitions have been used:

$$\sigma_q=\gamma_q2^{\frac{14}{5}}\frac{5\pi\sqrt{\pi}}{21}\varepsilon_0g_0d_p^3\left(\frac{\alpha_p}{V_p}\right)^2\cdot\Gamma\left(\frac{12}{5}\right)r^*\left(\frac{15m^*}{16Y^*\sqrt{r^*}}\right)^{\frac{2}{5}}\Theta_p^{\frac{9}{10}} \quad (2)$$

$$\kappa_{total}=\frac{d_p\sqrt{\Theta_\mathrm{p}}}{9\sqrt{\pi}g_0V_p}+\gamma_q2^{\frac{14}{5}}\frac{5\sqrt{\pi}}{21}g_0d_p^2\left(\frac{\alpha_p}{V_p}\right)^2\Gamma\left(\frac{12}{5}\right)r^*\left(\frac{15m^*}{16Y^*\sqrt{r^*}}\right)^{\frac{2}{5}}\Theta_p^{\frac{9}{10}} \quad (3)$$

### 2.3 Boundary Conditions for Charge

The boundary condition, as stated in [19], is given by

$$\sigma_{q,w}\left(\frac{\Delta\varphi}{\delta_ce}-\frac{2Q_p}{\pi\varepsilon_0d_p^2}\right)+\kappa_\mathrm{q}\mathbf{n}_\mathrm{w}\cdot\nabla Q_p-\left(\sigma_\mathrm{q}-\sigma_\mathrm{q,w}\right)\mathrm{E}\cdot\mathbf{n}_\mathrm{w}=0 \quad (4)$$

The first term represents the role of the work function difference at the boundary. Additionally, the second and third terms stand for diffusion and conduction contribution. As reported by Kolehmainen et al. [19], the nature of the solution to this problem is determined by the ratio of two timescales, one associated with tribo-charging, $\tau_e$, and the other representative of charge diffusion, $\tau_d$:

$$\tau_e=\frac{\varepsilon_0}{\sigma_q} \quad (5)$$

$$\tau_d=\frac{\alpha_pL^2}{\kappa_qV_p} \quad (6)$$

In the above equations, $L$ stands for a characteristic length of the system. If $\tau_e$ is much smaller than $\tau_d$, the diffusion term can be neglected (as the latter effects will affect the charge distribution insignificantly).

## 3 RESULTS

### 3.1 Unit test 1: Tribocharging Solver Testing

The correctness of the implemented code was tested for fixed physical properties (i.e. particle density, volume, diameter, heat capacity and thermal conductivity), solid volume fraction ($\alpha_p$) and granular temperature ($\Theta_p$). Therefore, the coefficients for the charge transport equation can be considered as fixed (i.e. $\sigma_q, \kappa_{total}$ are constant). With this assumption, one can rearrange Eqn. (1) as follows:

$$\frac{\alpha_p}{V_p}\partial_tQ_p+\frac{\alpha_p}{V_p}\nabla\cdot(Q_p\mathbf{u_p})=-\left(\sigma_q\frac{\alpha_pQ_p}{\varepsilon_0V_p}\right)+\kappa_{total}\Delta Q_p \quad (7)$$

The above equation contains a transient term and a convective term on the left-hand side, while the right-hand side comprises a conductive contribution caused by tribo-electrification and a diffusive contribution. To check the correctness of our implementation of this balance equation, we simulate two limiting cases: (i) pure conduction and (ii) pure diffusion inside a rectangular channel that spans $-96\,d_\mathrm{p} < x < 96\,d_\mathrm{p}$, $-6\,d_\mathrm{p} < y < 6\,d_\mathrm{p}$ and $-6\,d_\mathrm{p} < z < 6\,d_\mathrm{p}$. The channel is resolved by

a $50 \times 4 \times 4$ cartesian mesh and the equations are advanced with a constant time step of $\Delta t = 0.001\ s$. During all runs the granular temperature $\Theta_p$, the solid volume fraction $\alpha_p$ and the particle material properties are kept constant. In the conductive case, convection is suppressed ($U_x = 0$), electrical conductivity is finite ($\sigma_q \neq 0$) and electrical diffusivity is set to zero ($\kappa_q = 0$). In the diffusive case the opposite holds ($\sigma_q = 0, \kappa_q \neq 0$). Both scenarios start from an identical step-wise initial charge distribution, $Q_p(t=0) = 10^{-14}\ C\ m^{-3}$ with $-1$ for $x < 0$ and $+1$ for $x \geq 0$.

The diffusive case can be also verified by considering charge diffusion in a semi-infinite medium whose surface is maintained at a constant charge (i.e. $Q_0$). The charge is initially zero in this medium. The analytical solution for this case is given in Eq. (3.13) of Crank [20].

**Table 1. Physical properties of the particles.**

| *Name* | *Value* | *Unit* |
|---|---|---|
| Particle diam. ($d_p$) | 250 | [μm] |
| Particle density ($\rho_p$) | 2500 | $\left[\frac{kg}{m^3}\right]$ |
| Granular temperature ($\Theta_p$) | 0.01 | $\left[\frac{\mathrm{m}^2}{\mathrm{s}^2}\right]$ |
| Volume frac. ($\alpha_p$) | 0.15 | [−] |

### 3.1.1 Conductive case

In this case we just consider the conductive contribution, meaning that electrical diffusivity is ignored (i.e. $\kappa_{total} = 0$) and no convection is present ($\mathbf{u_p} = 0$) We can hence simplify to:

$$\partial_t Q_p = -\left(\frac{\sigma_q}{\varepsilon_0} Q_p\right) \qquad (8)$$

With the analytical solution becoming:

$$Q_p(t,x) = Q_0(x) e^{-\frac{\sigma_q}{\varepsilon_0} t} \qquad (9)$$

Figure 1 shows that, for the pure-conduction benchmark, the dimensionless charge profile $Q/Q_0$ keeps its initial top-hat shape along the normalised coordinate $x^*$ while its plateau levels decrease uniformly with time ($t^* = 10 - 60$). This is in line with the analytical solution of Eqn. (9) for a conduction-only process. Notably, the jump at $x^* = 0$ remains sharp and the plateaus do not spread, indicating that the solver adds virtually no numerical diffusion.

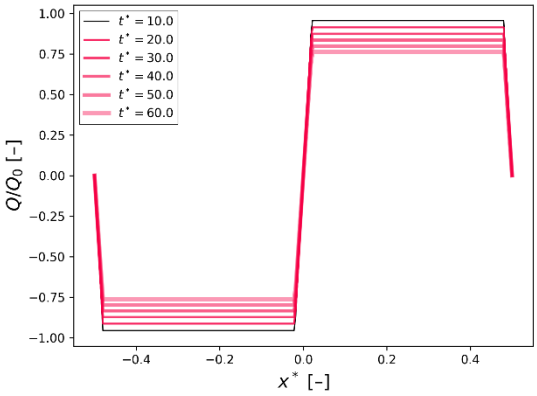


**Figure 1 Dimensionless charge ($Q/Q_0$) for the case with $\sigma_q$ calculated from physical properties from Table 1. The dimensionless time is defined as $t^* = t/\frac{L}{\sqrt{\theta}}$.**

Figure 2 represents an extreme case in which the electrical conductivity $\sigma_q$ was deliberately increased by three orders of magnitude. As a result, the characteristic relaxation time becomes much shorter than in the reference run, and the positive-and-negative charge plateaus level out almost immediately. While the charge step at $x^* = 0$ remains sharp, its amplitude collapses within a very brief period.

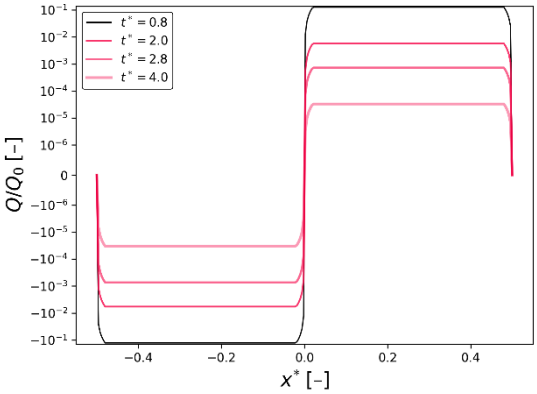


**Figure 2. Dimensionless charge distribution ($Q/Q_0$) for the case with $1000\sigma_q$ (with $\sigma_q$ calculated from the physical properties from Table 1). The dimensionless time is defined as $t^* = t/\frac{L}{\sqrt{\theta}}$.**

### 3.1.2 Diffusive case

In this case, just the diffusion contribution is considered, meaning that the electrical conduction term is ignored (i.e. $\sigma_q = 0$) and no convection is considered (i.e,. $\mathbf{u_p} = 0$). In such circumstances, we can write:

$$\partial_t Q_p = \kappa_{total} \frac{V_p}{\alpha_p} \Delta Q_p \qquad (10)$$

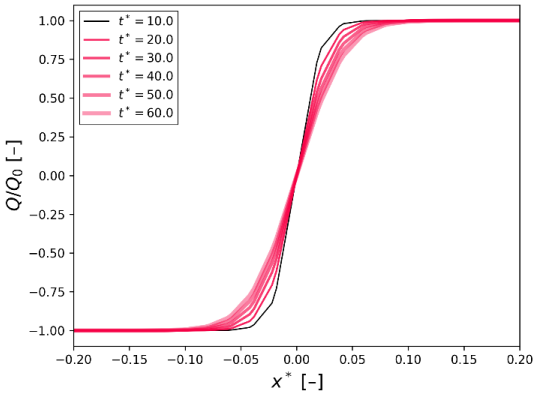


**Figure 3. Dimensionless charge ($Q/Q_0$) for the case with $\kappa_{total}$ calculated from physical properties of Table 1. The dimensionless time is defined as $t^* = t/\frac{L}{\sqrt{\theta}}$.**

Figure 3 shows that, for the pure-diffusion benchmark, the dimensionless charge profile $Q/Q_0$ evolves as expected: starting from the same top-hat distribution as before, the plateau values remain essentially constant while the step at $x^* = 0$ spreads symmetrically with increasing time $t^*$producing the S-shaped curves that follow the error-function form expected for a diffusion-controlled process.

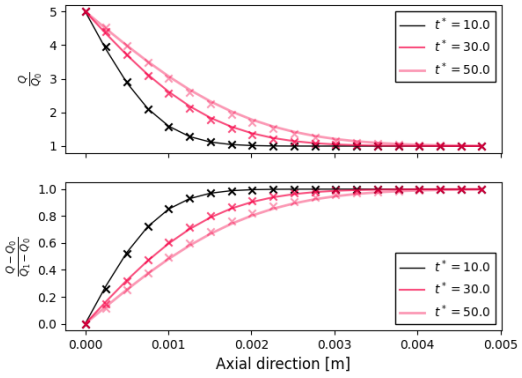


**Figure 4. Comparison of dimensionless charge distribution to the analytical solution for initial charge $Q_0 = 10^{-14}$ and a fixed charge $Q_1 = 5e^{-15}$ at the left boundary in an semi-infinite box, The dimensionless time is defined as $t^* = t/\frac{L}{\sqrt{\theta}}$.**

Figure 4 compares the simulated dimensionless charge profiles $Q/Q_0$ (symbols) with the analytical solution (solid lines) for the one–dimensional semi-infinite medium whose boundary at $x = 0$ is held at a constant charge $Q_0$. Results are shown for three dimensionless time coordinates. As can be seen, the diffusion front penetrates into the domain, and the simulation tracks the theoretical curves almost perfectly.

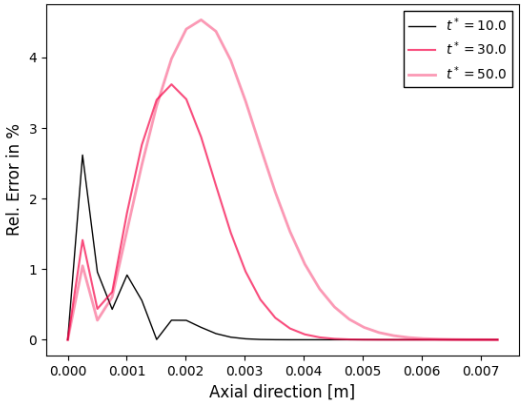


**Figure 5. Relative error of dimensionless charge $Q/Q_0$ for the case of an semi-infinite half plane, The dimensionless time is defined as $t^* = t/\frac{L}{\sqrt{\theta}}$.**

Figure 5 presents the corresponding relative error along the axial direction. The error peaks close to the charged wall, but decays rapidly with distance and time, falling below 1 % in the bulk of the domain. Together the two plots confirm that the solver reproduces the analytical solution with high accuracy.

## 3.2 Unit Test 2: Nozzle flow

Unit test 2 benchmarks the flow through a canonical converging–diverging nozzle (with geometric parameters $\Theta = 5.7\,°$, $D_b = 40\,mm$, $D_h = 28\,mm$, $D_e = 37.46\,mm$, and $L = 47.4\,mm$, as well as simulation parameters $\gamma = 1.4$, $R_s = 286.71\,{}^{J}/_{kg\,.\,K}$, and $p_t = 6e5\,Pa$) to compare the performance of two different OpenFOAM® solvers. Figure 6 contrasts the temperature and velocity fields generated by the single-phase compressible solver „rhoReactingBuoyantFoam" (upper row) with those from the „two-phase-capable reactingTwoPhaseEulerFoam" (bottom row).

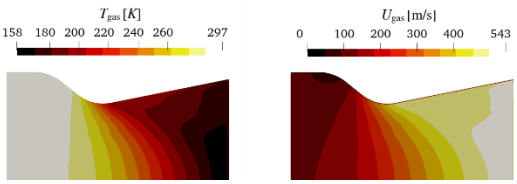


**Figure 6. Simulated gas flow through a converging–diverging nozzle (flow direction is left to right). (a, c) gas temperature $T_{gas}$ [$K$]; (b, d) gas velocity magnitude $U_{gas}$ [$\frac{m}{s}$]. Results in the top row (a, b) were obtained with the compressible solver rhoReactingBuoyantFoam (RRBF), while the bottom row (c, d) employs the solver reactingTwoPhaseEulerFoam (RTPEF).**

In both solutions predicted by the solvers the gas accelerates from sub-sonic conditions upstream of the throat to a supersonic jet at the exit: the colour maps show a smooth rise in velocity to about $543\ m/s$ for the solver RRBF and $533\ m/s$ for RTPEF. The core flow cools down to $158\ K$ for both cases. These outlet values match the one-dimensional analytical estimates listed in Table 2 within a few percent, while any discrepancies between the two numerical approaches are most likely confined to the wall regions. The unit test thus confirms that the „reactingTwoPhaseEulerFoam" reproduces compressible-flow behaviour with the same level of accuracy as the established single-phase solver, providing a reliable foundation for subsequent gas–particle simulations.

**Table 2. Analytical results for nozzle flow according to the model of Kong et al. [21].**

| *Name* | *Unit* | *Value* |
|---|---|---|
| Gas temperature at the outlet $T_{g,e}$ | $[K]$ | 161.6 |
| Gas velocity at the outlet $U_{g,e}$ | $\left[\frac{m}{s}\right]$ | 527.1 |

## 4 BENCHMARK: FORWARD-FACING STEP

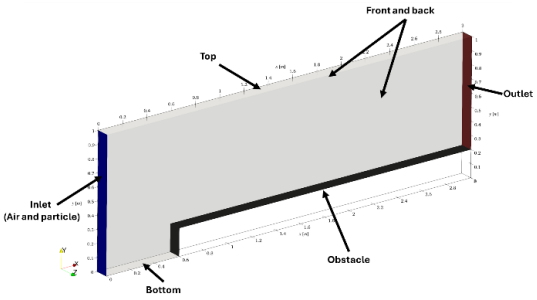


**Figure 7. The geometry of the forward facing showcase.**

We now shift our attention to a show case that illustrates the combined use of the flow and tribocharging solver. As shown in Figure 7, the air and particles would enter the domain from the inlet patch and would leave it via the outlet patch. The flow is confined by an obstacle which is defined as a wall. The top and bottom patches are symmetry planes, and the front and back faces were defined as "empty". The particles and the gas enter the domain with a fixed velocity of $(50,0,0)\ \frac{m}{s}$ with a volume fraction of $\alpha_p = 4.8 \cdot 10^{-4}$, as well as a temperature of $1000\ K$. The particle diameter is $d_p = 136\ \mu m$. The particle will get charged when hitting the obstacle surface with a work function difference of $1\ eV$. Figure 8 shows the results after a flowtime of $1\ s$. As it can be seen, the particles just above the obstacle's surface have a substantially higher-charge than the particles in other regions. However, the particle volume fraction in this high charge region is much smaller than at other locations. This can be explained by the flow condition affected by the obstacle's shape.

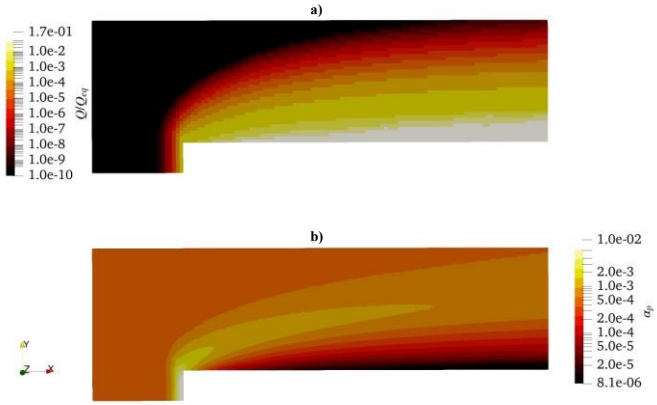


**Figure 8. Results for the forward facing showcase: a) dimensionless charge, b) particle volume fraction contour plots.**

## 5 CONCLUSIONS

We demonstrated the functionality of a newly implemented triboelectrification solver in the popular open-source environment OpenFOAM®. Also, appropriate boundary conditions were implemented. Specifically, this was done for two sets of unit test scenarios, as well as a showcase.

The latter case highlights a strongly heterogeneous net particle charge distribution. This may lead to the development of strong electric fields, and hence the danger of local arcing phenomena in practical applications.

For the unit test cases, a $k-\varepsilon$ turbulence model was applied to ensure robustness of the solver under weakly fluctuating conditions. In contrast, the nozzle-flow simulation employed a $k-\omega$ SST model, while the showcase simulation was conducted under laminar assumptions. In future studies, it would be potentially beneficial to apply high-fidelity turbulence-resolving approaches, such as Large Eddy Simulation (LES) or Direct Numerical Simulation (DNS), to better assess the interaction between turbulent fluctuations and triboelectric charge transport: the recent study of Croquer et al. [22] showed that LES does not offer advantages with repect to time averaged quantaties (compared to RANS data) for a similar flow situation. However, at turbulent fluctuations can be directly predicted by LES, which is not the case for RANS. Hence, using LES potentially is better suited to predict particle-wall collisions and hence triboelectrification.

Future work will (and has partially already) apply the solvers to relevant industry-scale problems in the field of battery venting channel design.

## 6 ACKNOWLEDGEMENTS

This work was financially supported by the Austrian Research Promotion Agency (FFG) through the projects "PREVENT+" and "Safe Sustain". PREVENT+ was funded under the program *"Mobilität der Zukunft"*, while SafeSustain was supported by the program *"Mobilitätstechnologie"* of the Austrian Federal Ministry for Innovation, Mobility and Infrastructure (BMIMI).

This publication was prepared at Virtual Vehicle Research GmbH in Graz and received partial funding within the COMET K2 Competence Centers for Excellent Technologies. The COMET program is funded by the Austrian Federal Ministry for Innovation, Mobility and Infrastructure (BMIMI), the Austrian Federal Ministry for Economy, Energy and Tourism (BMWET), the Province of Styria (Department 12), and the Styrian Business Promotion Agency (SFG). Programme management has been entrusted to the Austrian Research Promotion Agency (FFG).


For improving readability and language style, AI-based tools were utilized during manuscript preparation. The content and scientific arguments presented remain entirely the responsibility of the authors.

## 7 REFERENCES

[1] S. Matsusaka, H. Maruyama, T. Matsuyama, and M. Ghadiri, "Triboelectric charging of powders: A review," *Chemical Engineering Science*, vol. 65, no. 22, pp. 5781–5807, Nov. 2010, doi: 10.1016/j.ces.2010.07.005.

[2] S. Naik, R. Mukherjee, and B. Chaudhuri, "Triboelectrification: A review of experimental and mechanistic modeling approaches with a special focus on pharmaceutical powders," *International Journal of Pharmaceutics*, vol. 510, no. 1, pp. 375–385, Aug. 2016, doi: 10.1016/j.ijpharm.2016.06.031.

[3] Y. Zhang, P. Ping, X. Ren, W. Gao, D. Kong, and X. Yin, "Characteristics and generation mechanism of ejecta-induced arc for lithium-ion battery during thermal runaway," *eTransportation*, vol. 24, p. 100429, May 2025, doi: 10.1016/j.etran.2025.100429.

[4] C. Cimarelli and K. Genareau, "A review of volcanic electrification of the atmosphere and volcanic lightning," *Journal of Volcanology and Geothermal Research*, vol. 422, p. 107449, Feb. 2022, doi: 10.1016/j.jvolgeores.2021.107449.

[5] N. O. Renno *et al.*, "MATADOR 2002: A pilot field experiment on convective plumes and dust devils," *Journal of Geophysical Research: Planets*, vol. 109, no. E7, 2004, doi: 10.1029/2003JE002219.

[6] A. T. Ndama, P. Guigon, and K. Saleh, "A reproducible test to characterise the triboelectric charging of powders during their pneumatic transport," *Journal of Electrostatics*, vol. 69, no. 3, pp. 146–156, Jun. 2011, doi: 10.1016/j.elstat.2011.03.003.

[7] S. Golshan, R. Sotudeh-Gharebagh, R. Zarghami, N. Mostoufi, B. Blais, and J. A. M. Kuipers, "Review and implementation of CFD-DEM applied to chemical process systems," *Chemical Engineering Science*, vol. 221, p. 115646, Aug. 2020, doi: 10.1016/j.ces.2020.115646.

[8] J. Kolehmainen, A. Ozel, and S. Sundaresan, "Eulerian modelling of gas–solid flows with triboelectric charging," *J. Fluid Mech.*, vol. 848, pp. 340–369, Aug. 2018, doi: 10.1017/jfm.2018.361.

[9] W. Xu and H. Grosshans, "Experimental study of humidity influence on triboelectric charging of particle-laden duct flows," *Journal of Loss Prevention in the Process Industries*, vol. 81, p. 104970, Feb. 2023, doi: 10.1016/j.jlp.2022.104970.

[10] R. D. Cruise, S. O. Starr, K. Hadler, and J. J. Cilliers, "Triboelectric charge saturation on single and multiple insulating particles in air and vacuum," *Sci Rep*, vol. 13, no. 1, p. 15178, Sep. 2023, doi: 10.1038/s41598-023-42265-0.

[11] D. Liu *et al.*, "Standardized measurement of dielectric materials' intrinsic triboelectric charge density through the suppression of air breakdown," *Nat Commun*, vol. 13, no. 1, p. 6019, Oct. 2022, doi: 10.1038/s41467-022-33766-z.

[12] F. O. Alfano, A. Di Renzo, F. P. Di Maio, and M. Ghadiri, "Computational analysis of triboelectrification due to aerodynamic powder dispersion," *Powder Technology*, vol. 382, pp. 491–504, Apr. 2021, doi: 10.1016/j.powtec.2021.01.011.

[13] H. Grosshans, "Influence of weak electrostatic charges and secondary flows on pneumatic powder transport," *Can J Chem Eng*, vol. 101, no. 5, pp. 2347–2360, May 2023, doi: 10.1002/cjce.24824.

[14] M. Zeybek and H. Grosshans, "Eulerian formulation for the triboelectric charging of polydisperse powder flows," *Physics of Fluids*, vol. 33, no. 6, p. 063304, Jun. 2021, doi: 10.1063/5.0054374.

[15] C. Montilla, R. Ansart, and O. Simonin, "Charge–velocity correlation transport equations in gas–solid flow with triboelectric

effects," *J. Fluid Mech.*, vol. 955, p. A22, Jan. 2023, doi: 10.1017/jfm.2022.1054.
[16] M. Ray, F. Chowdhury, A. Sowinski, P. Mehrani, and A. Passalacqua, "Eulerian modeling of charge transport in bi-disperse particulate flows due to triboelectrification," *Physics of Fluids*, vol. 32, no. 2, p. 023302, Feb. 2020, doi: 10.1063/1.5140473.
[17] C. Y. Wen and Y. H. Yu, "Mechanics of fluidization," in *Fluid-Particle Technology*, vol. 62, in Chemical Engineering Progress Symposium Series, vol. 62. , New York: American Institute of Chemical Engineers, pp. 100–111.
[18] P. C. Johnson and R. Jackson, "Frictional–collisional constitutive relations for granular materials, with application to plane shearing," *Journal of Fluid Mechanics*, vol. 176, pp. 67–93, Mar. 1987, doi: 10.1017/S0022112087000570.
[19] J. Kolehmainen, L. Ceresiat, A. Ozel, and S. Sundaresan, "110th Anniversary: Effect of System Size on Boundary-Driven Contact Charging in Particulate Flows," *Ind. Eng. Chem. Res.*, vol. 58, no. 38, pp. 17980–17990, Sep. 2019, doi: 10.1021/acs.iecr.9b03437.
[20] J. Crank, *The mathematics of diffusion*, 2. ed., Reprint. Oxford: Clarendon Press, 1976.
[21] D. Kong, G. Wang, P. Ping, and J. Wen, "A coupled conjugate heat transfer and CFD model for the thermal runaway evolution and jet fire of 18650 lithium-ion battery under thermal abuse," *eTransportation*, vol. 12, p. 100157, May 2022, doi: 10.1016/j.etran.2022.100157.
[22] S. Croquer, O. Lamberts, S. Poncet, S. Moreau, and Y. Bartosiewicz, "Large Eddy Simulation of a supersonic air ejector," *Applied Thermal Engineering*, vol. 209, p. 118177, Jun. 2022, doi: 10.1016/j.applthermaleng.2022.118177.